# Multiple twins of a decagonal approximant embedded in S-Al$_2$CuMg phase resulting in pitting initiation of a 2024Al alloy

J. Wang,[1] B. Zhang,[1] Y.T. Zhou and X.L. Ma[*]

*Shenyang National Laboratory for Materials Science, Institute of Metal Research, Chinese Academy of Sciences,
Wenhua Road 72, 110016 Shenyang, People's Republic of China*

**Abstract**—The pitting of Al–Cu–Mg alloy is believed to originate from the local dissolution of S-Al$_2$CuMg particles, and the dissolution activity differs from one particle to another. Nevertheless, the initial site where the dissolution of the S phase preferentially occurs and the cause of the heterogeneity in the electrochemical dissolution activity remain unknown, hindering our understanding of pitting initiation of Al–Cu–Mg alloys. In this work, we have applied in situ ex-environmental transmission electron microscopy and identified a large number of nanosized Al$_{20}$Cu$_2$Mn$_3$ approximants of the decagonal quasicrystal embedded in the S phase. We find that the S phase with Al$_{20}$Cu$_2$Mn$_3$ inclusions is more active than those free of the approximants. Such a preference is clarified to result from the decomposition of Al$_{20}$Cu$_2$Mn$_3$ approximant prior to the dissolution of the S phase. In addition, we also find that the electrochemical behavior of Al$_{20}$Cu$_2$Mn$_3$ approximants is different. The approximants with multiple twins are more active than those with few planar defects.
© 2014 Acta Materialia Inc. Published by Elsevier Ltd. All rights reserved.

*Keywords:* S phase; Pitting; Al$_{20}$Cu$_2$Mn$_3$; 2024Al; Multiple twins

## 1. Introduction

Al–Cu–Mg alloys (2xxx series commercial alloys) are widely used in aerospace and other industrial applications because of their combination of strength, damage tolerance, formability and density. Al–Cu–Mg alloys derive their strength from a heterogeneous microstructure that consists of hardening precipitates and dispersoids [1,2]. However, they are prone to localized corrosion, and thus premature breakdown may occur when they are used in a chloride-containing environment.

In the past few decades, researchers have been striving to study the pitting of Al–Cu–Mg alloy using various techniques [3–8]. Among various second-phase particles present in Al–Cu–Mg alloy, attention is usually paid to the influence of the S-Al$_2$CuMg phase, which is believed to dissolve preferentially as the initiation sites of pitting [9–15]. The S phase is one of the key strengthening precipitates in high-strength Al–Cu–Mg alloys and has an orthorhombic structure with space group *Cmcm* [16–21]. In previous studies, the mechanism of pitting corrosion occurring at the S phase was believed to be as follows. The S phase is electrochemically active with respect to the matrix and it is dissolved initially as an anode with Mg and Al selective

dissolution. With the development of Mg and Al dealloying, the remnant becomes noble and tends to behave as a cathode, which results in the dissolution of the matrix around the S phase and consequently pitting occurrence [10,12,22]. In addition, the S phase particles are known to feature a great heterogeneity in electrochemical activity. In the chloride-containing electrolyte, some S particles are susceptible to dissolution, while others are electrochemically inactive. Moreover, the dissolution of a so-called active S particle usually occurs in an inhomogeneous manner. The intrinsic mechanism has not yet been clarified, which limits our understanding of pitting initiation in Al–Cu–Mg alloys [7,23]. Such an unpredictable phenomenon must result from the poor knowledge of microstructural information which is derived from the relatively lower spatial resolution of analysis tools or modes, such as scanning electron microscopy (SEM), bright-field transmission electron microscopy (TEM), energy dispersive X-ray spectroscopy (EDXS), standard electrochemical measurements, scanning vibrating electrode (SVE) and scanning Kelvin probe force microscopy (SKPFM), as well as secondary ion mass spectroscopy (SIMS) [8–13,23].

In this work, we have applied an in situ ex-environmental TEM technique [24] to clarify the pitting initiation of an 2024Al alloy. We provide atomic-scale information on the initial site of S phase dissolution and show a novel interpretation of the classical problem, which has been unresolved for decades.

---

\* Corresponding author; e-mail: xlma@imr.ac.cn

[1] These authors contributed equally to this work.

## 2. Experimental procedure

### 2.1. Sample preparation

2024 aluminum alloy with nominal composition of Al–4.35Cu–1.55Mg–0.53Mn–0.11Fe–0.13Si–0.03Ti (wt.%) was chosen for the investigation. The alloy was subjected to solid-solution treatment (SST) at 768 K and water quenching. After SST, the alloy was cold-drawn into a tube form at room temperature with shrinkage of 8–15%, and then was annealed at 380 °C for 1 h. The sample was cut into sections perpendicular to the deformation direction using a linear precision saw with a thickness of 600 μm and then ground to ∼100 μm thick by 1000 grit silicon carbide papers. Disks with a diameter of 3 mm were prepared by die-cutting, then ground using variant grit silicon carbide papers, polished with diamond paste to 20 μm and finally thinned by ion-milling. After the first-round TEM observation, some of the specimens were plasma-cleaned and then immersed in the $0.5 \, \text{mol} \, l^{-1}$ NaCl solution at room temperature for various periods (the duration ranged from 8 to 60 min). The TEM specimens which experienced the immersion tests were cleaned in distilled water, dried, plasma-cleaned and then transferred into the TEM for further investigation, and this was designated as the in situ ex-environmental TEM method.

### 2.2. SEM and TEM characterizations

An FEI field emission scanning electron microscope was used to observe the morphology of precipitates. A Tecnai G2 F30 transmission electron microscope, with a point resolution of 0.19 nm, equipped with a high-angle angular-dark-field (HAADF) detector and X-ray energy-dispersive spectrometer (EDS) systems, was used at 300 kV for electron diffraction, HAADF imaging, high-resolution electron microscopy (HREM) imaging and composition analysis.

## 3. Results and discussion

### 3.1. Heterogeneous dissolution of S phase

Fig. 1a is an SEM image showing the distribution of the second phase in the present 2024Al alloy. A combination of electron diffraction and EDS analysis (not shown here) indicates that the sample is mainly composed of three kinds of second-phase particles, e.g. S-$Al_2CuMg$ (at.%: Al 50.5, Cu 28.4, Mg 21.1), θ-$Al_2Cu$ (at.%: Al 60.7, Cu 39.3) and Al–Cu–Fe–Mn–Si (at.%: Al 62.8, Cu 7.6, Mn 10.4, Fe 14.5, Si 4.7) phase. The at.% of each element in every second phase is the average value from ten particles. The S phase particles account for ∼60% of the whole second phases.

An in situ ex-environmental TEM method and HAADF technique in the TEM are employed in this study. The HAADF mode provides incoherent images and uses high-angle scattering, leading to strong atomic number (Z) contrast. Therefore the image contrast in such a mode is strongly associated with the local variety of chemical composition and/or thickness contribution [25]. By repeated observation of a fixed TEM specimen of 2024Al alloy before and after immersion for varying durations (several tens of min) in $0.5 \, \text{mol} \, l^{-1}$ NaCl solution, we monitor the local microstructural evolution of a settled S phase particle.

The structural characteristics of the S phases before and after dissolution are particularly focused, and a typical example is shown in Fig. 1. Fig. 1b is the HAADF image of an S phase particle while Fig. 1c is the same particle that has been immersed in $0.5 \, \text{mol} \, l^{-1}$ NaCl for 15 min. The dissolution of the S phase results in a darker contrast (thickness contribution), from which the dissolution within the S phase is seen to be strongly localized with some small pits. They are distributed randomly and always feature a nanocore with a different contrast. Fig. 1d(I–XII) and e(I–XII) are the zoom-in images of the local area in Fig. 1b and c, showing the same areas in specimens before (Fig. 1d(I–XII)) and after immersion (Fig. 1e(I–XII)). It is of great interest to find that each core appears to correspond to one nanoparticle embedded in the S phase. These nanoparticles show slightly brighter contrast than the S phase matrix before immersion, while they show darker contrast than the dissolved S phase after immersion in NaCl, which indicates that the nanoparticles are dissolved more severely than the S phase particle. It seems that the local dissolution of the S phase is strongly correlated with the nanoparticle and the initial site of dissolution is at the periphery of the nanoparticle.

A number of HAADF images of S phase particles after suffering local dissolution are displayed in Fig. 2 with the same magnification. These pits and S phase particles show various dimensions and geometric projections, but each pit forms around a nanoparticle, no matter whether it is located at the inner part of or at the edge of S phase. It is seen that the dissolution of the S phase around most of the nanoparticles seems to concentrically propagate into the S phase.

Various TEM techniques are applied to identify crystallographic characteristics of the nanoparticles embedded in the S phase. The lattice type of these fine particles is determined on the basis of electron diffraction experiments. By observing dozens of S phase particles in TEM, it is confirmed that most S phase particles feature nanoparticle inclusions. Such nanoparticles are also dispersed in the Al matrix with a similar size to those in the S phase. A bright-field TEM image of an S phase is shown in Fig. 3a. The S phase is distinguished by combining EDS and electron diffraction patterns (EDPs). Fig. 3b is a series of EDPs obtained from S phase particles. The space group $Cmcm$ with lattice parameters of $a = 0.40$ nm, $b = 0.92$ nm and $c = 0.71$ nm is derived based on the extinction rules in the EDPs, which agrees with previous studies [16–21]. In Fig. 3a, four nanoparticles with sizes of 20–200 nm embedded in the S phase are arrowed and labeled as I, II, III and IV. It is seen from the zoom-in images of the nanoparticles in Fig. 3c that multiple twins are present in these nanoparticles and they are distinguished in two types of configuration: parallel shaped twin plates (Fig. 3c(I and II)) and prism shaped twin plates (Fig. 3c(III and IV)).

One typical nanoparticle with prism shaped plates (as shown in Fig. 4a) is selected for detailed TEM characterization. The darker contrast of the particle in this bright-field mode indicates that they are parallel or close to a low-indexed zone axis. The EDP (as seen in Fig. 4b) shows a pseudo-ten-fold symmetry and the EDS analysis (seen in Fig. 4c) indicates that the nanoparticle is composed of Al, Cu and Mn. To further identify the nanoparticle, a HRTEM image (Fig. 4d) is acquired. The nanoparticle is composed of twins with a rotation of nearly 36°. The crystal which has such a pseudo-tenfold symmetry is an
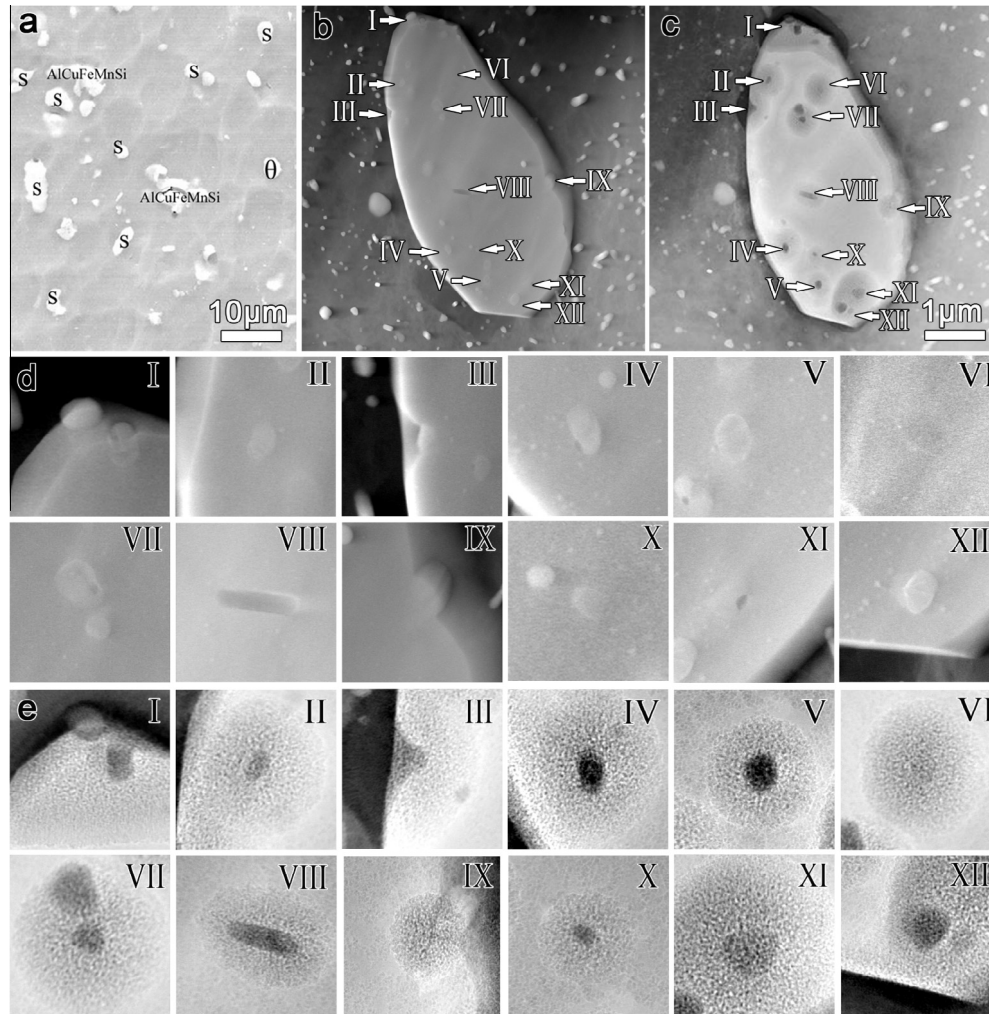
**Fig. 1.** In situ ex-environmental TEM observation showing the local dissolution of S phase. (a) An SEM image of the as-received 2024Al showing coarse intermetallic particles: S(Al$_2$CuMg), θ(Al$_2$Cu) and Al–Cu–Mn–Fe phases. (b) A HAADF image showing an S phase particle. (c) The same particle as that in (b) but after being immersed in 0.5 mol l$^{-1}$ NaCl for 15 min. (d) Zoom-in images showing 12 nanoparticles embedded in the S phase in (b). (e) Zoom-in images showing local dissolution around these nanoparticles in (c).

approximant of a decagonal quasicrystal (DQC) [26,27]. The DQC and its crystalline approximants share similar structural units, which are stacked aperiodically in the former but periodically in the latter. The approximant of the DQC in 2024Al alloy is Al$_{20}$Cu$_2$Mn$_3$ with space group *Bbnm* and lattice parameters of $a = 2.42$ nm, $b = 1.25$ nm and $c = 0.775$ nm [1,28–31]. The HRTEM micrograph and the EDP in Fig. 4d and b of Al$_{20}$Cu$_2$Mn$_3$ are obtained along the crystallographic [0 1 0] direction and the twin planes are all {1 0 1}. The Al$_{20}$Cu$_2$Mn$_3$ is formed during the homogenization process of Al alloy and cannot be dissolved in subsequent heat treatment [1]. Such uniformly distributed fine Al$_{20}$Cu$_2$Mn$_3$ dispersoids are frequently observed and they are present in many other aluminum alloys. Owing to the fine dimension and complex crystallographic structure, the dispersoids are known to improve the mechanical properties of aluminum alloys [32,33]. However, the electrochemical effect of Al$_{20}$Cu$_2$Mn$_3$ has been little understood, probably due to the lack of high-resolution techniques for the direct observation of local corrosion. It is not straightforward to observe the nanosize Al$_{20}$Cu$_2$Mn$_3$ particles embedded in the S phase since the contrast

difference between the S phase and Al$_{20}$Cu$_2$Mn$_3$ is subtle in bright-field TEM and even in the HAADF mode.

After observing dozens of S phases in specimens, we find that the dissolution activity between S phase particles is highly heterogeneous. Such a difference in activity has already been found in previous studies [7,23], but the substantial mechanism has not been clarified yet. In the specimen immersed in 0.5 mol l$^{-1}$ NaCl solution for 45 min, most S phase particles are dissolved severely, while some remain unchanged. This indicates that S phase particles are electrochemically different. We find that the S phase particles free of or with few Al$_{20}$Cu$_2$Mn$_3$ nanoparticles usually do not suffer local dissolution. Fig. 5 shows two typical samples of undissolved S phase particles and their EDS mapping images, from which the two particles are seen to be free of Al$_{20}$Cu$_2$Mn$_3$. Although several Al–Cu–Mn–Fe containing particles exist at the boundary, they do not induce any dissolution of the S phase. Therefore, it is the Al$_{20}$Cu$_2$Mn$_3$ approximant that makes the difference in S phase activity. In other words, the S phases with Al$_{20}$Cu$_2$Mn$_3$ approximant are more active, while those free of or with few nanoparticles are inactive at the early stage of corrosion.
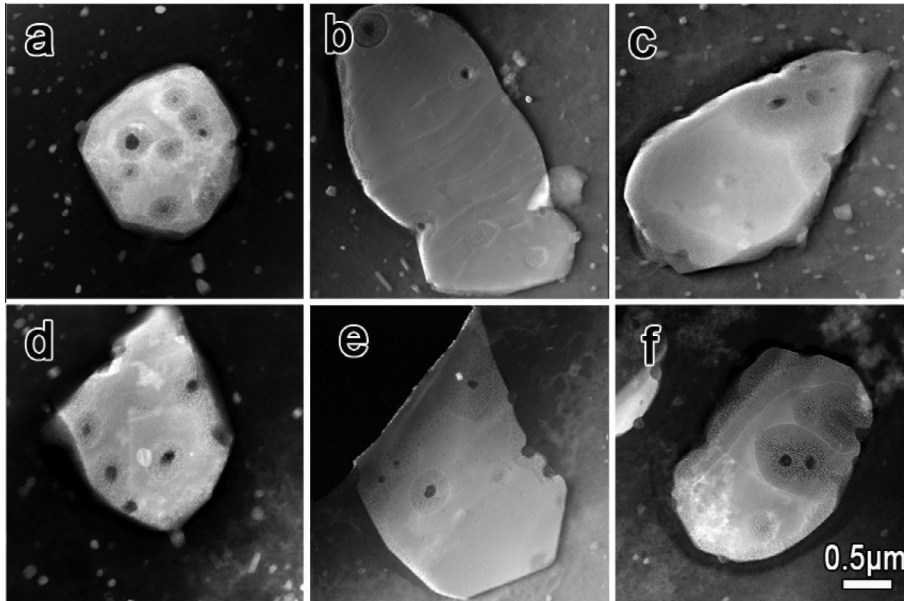
**Fig. 2.** HAADF images of S phase particles in which local dissolution occurred and pits formed around the nanoparticles. These images have the same magnification and were obtained from the specimens immersed in 0.5 mol l$^{-1}$ NaCl for 8–25 min.
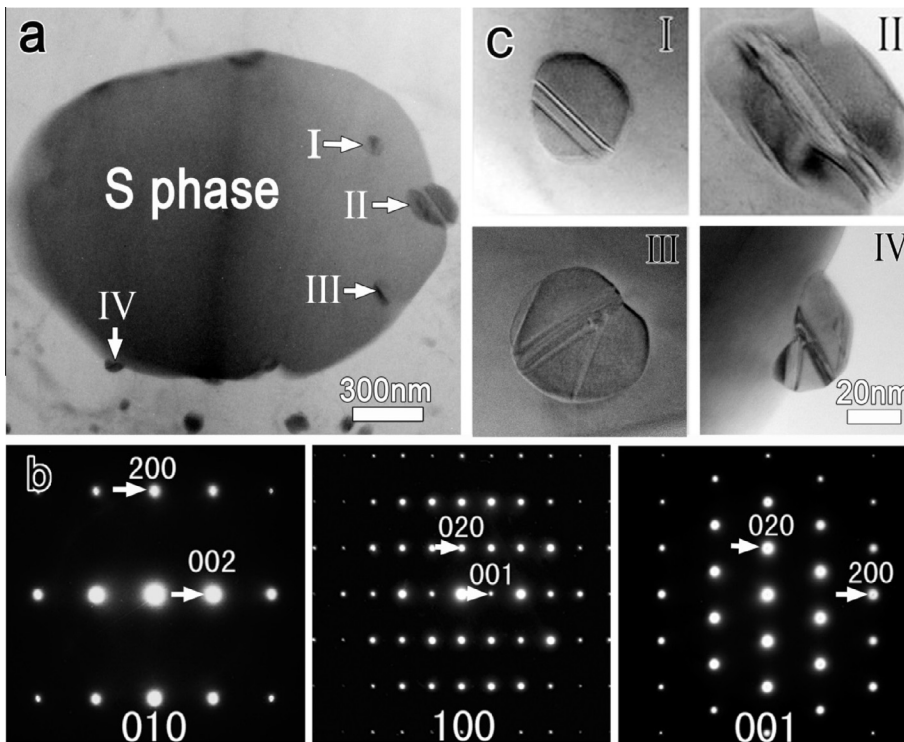


**Fig. 3.** TEM observation of S phase particle. (a) Bright-field TEM image in which four nanoparticles embedded in an S phase are arrowed. (b) EDPs of S phase with zone axis of [010], [100] and [001]. (c) Zoom-in bright-field TEM images of the nanoparticles in (a) labeled as I, II, III and IV.

## 3.2. Development process of localized corrosion

The HAADF images shown in Fig. 6 illustrate the continuous development of local dissolution of the S phase and the resultant dissolution of the Al matrix. First, the $Al_{20}Cu_2Mn_3$ phase rather than the S phase appears active and is dissolved initially. As shown in Fig. 6a, three $Al_{20}Cu_2Mn_3$ particles (arrowed) embedded in an S phase are dissolved locally and small pits are left behind, while the surrounding S phase remains unchanged. Second, the small pit formed by the dissolution of $Al_{20}Cu_2Mn_3$ is enlarged by the dissolution of the S phase at the periphery of dissolved $Al_{20}Cu_2Mn_3$, and $Al_{20}Cu_2Mn_3$ is subsequently dissolved severely, as shown with the darker contrast in Fig. 6b. Third, when the pit reaches the boundary of the S phase/matrix, the dissolution develops along the
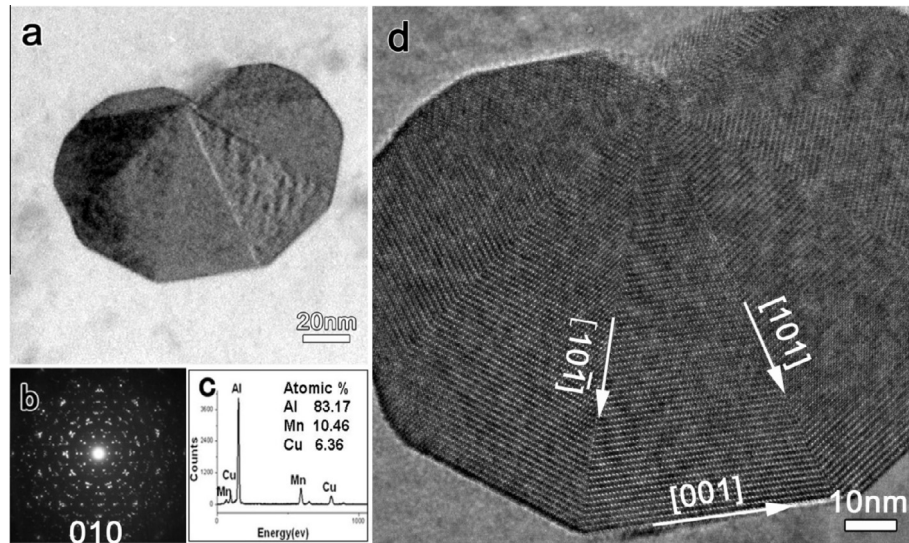
**Fig. 4.** Identification of the nanoparticle. (a) Bright-field TEM image of the nanoparticle. (b) EDP obtained from the nanoparticle in (a). (c) EDS analysis of the particle is composed of Al, Mn and Cu. (d) HRTEM image along the same axis in (b).
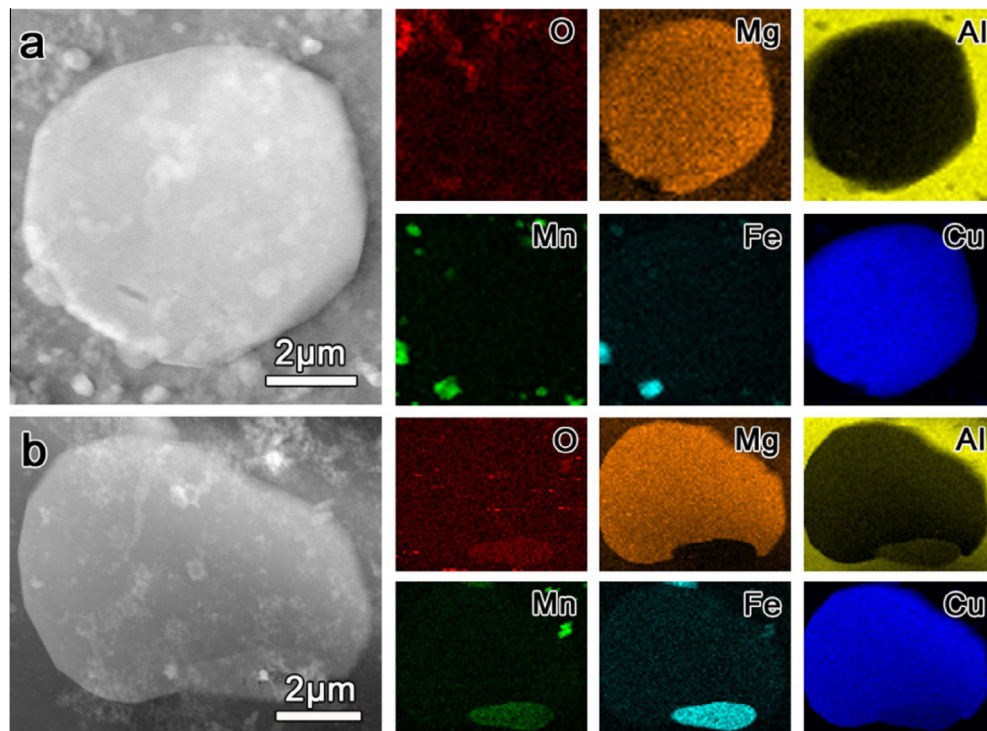


**Fig. 5.** HAADF images showing two undissolved S phase particles in 2024Al after being immersed in $0.5 \, mol \, l^{-1}$ NaCl for 45 min and their EDS mapping images.

boundary quickly (shown in Fig. 6c) as a result of the coupling effect between the S phase (anode) and Al matrix (cathode), while the extending around the $Al_{20}Cu_2Mn_3$ remnant becomes minor. The dissolved S phase, with Mg and Al dealloying, tends to change from anodic to cathodic with respect to the Al matrix and the local pH near the matrix becomes more alkaline because of the cathodic reaction, resulting in the dissolution of the adjacent Al matrix (shown in Fig. 6c). Finally, based on the characters of corrosion morphology shown in Fig. 6d, the most severe corrosion is identified in zone I, mild corrosion in zone II

and no corrosion in zone III. Such morphology implies that once the dissolution of the S phase reaches and subsequently develops along the boundary, the dissolution is extended from its periphery to the interior. Meanwhile, the dissolution in the Al matrix further extends outward. In other words, the cathodic S phase remnant ring, which is formed by the dissolution of the S phase particle along the boundary, both causes the Al matrix to dissolve and continues accelerating the S phase dissolution to extend into the interior. The dissolution of $Al_{20}Cu_2Mn_3$ located at or near the boundary results in the extending of S phase

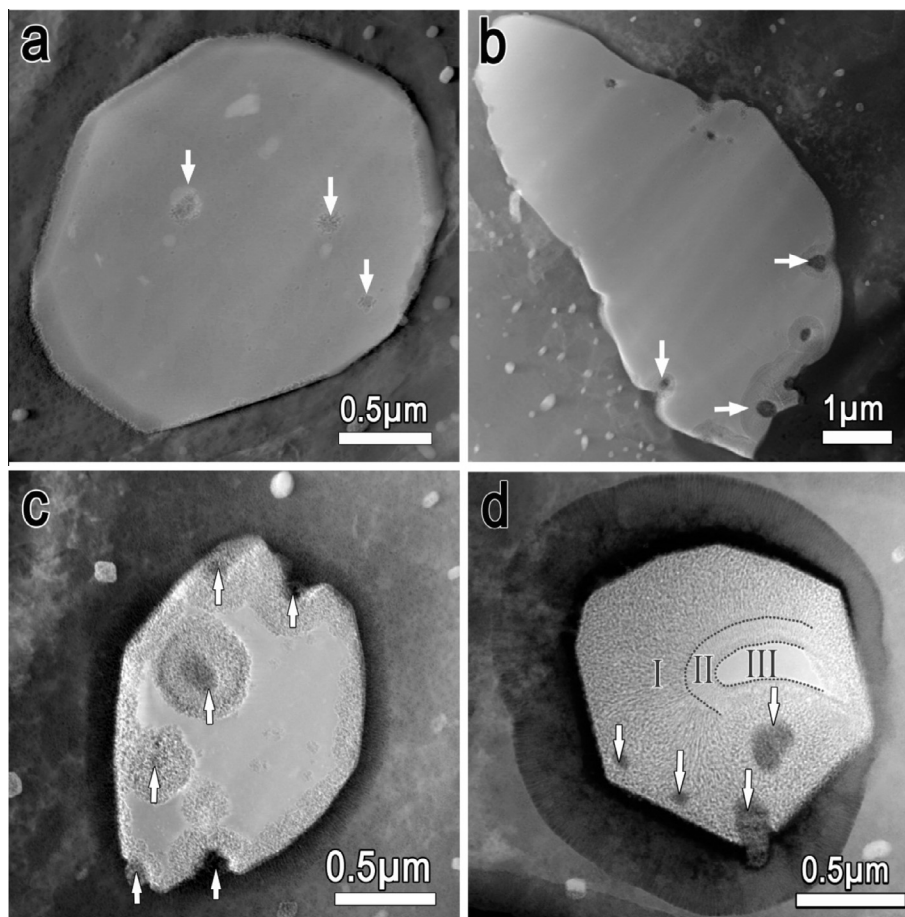**Fig. 6.** Observation of the continuous development of local dissolution of S phase and the resulting dissolution of Al matrix. The $Al_{20}Cu_2Mn_3$ particles are arrowed. (a) A HAADF image showing that slight local dissolution occurs and that fine pits form at the $Al_{20}Cu_2Mn_3$. (b) Pits enlarge to the S phase at the periphery of dissolved $Al_{20}Cu_2Mn_3$. (c) When the pits are extended to reach the boundary of S phase/matrix, the dissolution develops along the boundary quickly and results in the dissolution of the adjacent Al matrix. (d) The cathodic S-phase remnant causes the Al matrix to dissolve and also to continue accelerating the S-phase dissolution to extend into the interior.

dissolution to quickly reach the boundary of the S phase/Al matrix, and thus results in the rapid dissolution of the adjacent Al matrix. Therefore, the $Al_{20}Cu_2Mn_3$ nanoparticles located at or near the boundary lead to the occurrence of Al matrix dissolution more effectively than when they are in the interior.

As the strengthening dispersoids in 2024Al, most of the $Al_{20}Cu_2Mn_3$ particles disperse in the Al matrix, but the electrochemical behavior of $Al_{20}Cu_2Mn_3$ in the matrix is totally different from those in the S phase. By observing the images shown in Figs. 1 and 2, a large number of $Al_{20}Cu_2Mn_3$ dispersoids are seen to disperse in the matrix. When the $Al_{20}Cu_2Mn_3$ particles in the S phase are dissolved severely, it is hard to find the dissolution of the $Al_{20}Cu_2Mn_3$ particles in the matrix. At a high resolution, only slight dissolution is found in some of them. Fig. 7 is an HAADF animage showing three locally dissolved $Al_{20}Cu_2Mn_3$ particles in the Al matrix with variant corroded degrees. The dissolution occurs in the interior randomly and it does not propagate further, which indicates that the local dissolution is retarded greatly. Although some trace-dissolution dots are seen to distribute in the adjacent matrix, evidently it is not due to the dissolved nanoparticle but a minor process triggered by the nearby cathodic S phase rem-

nant. So, the $Al_{20}Cu_2Mn_3$ remnant, different from the S phase, does not seem to switch from anode to cathode with respect to the Al matrix.

To fully understand the effect of locally dissolved $Al_{20}Cu_2Mn_3$ in the early corrosion stage, we analyze the chemical composition of a single pit in the S phase. Fig. 8 shows an S phase with local dissolution and its EDS mapping on a pit. The corroded core is composed of Al, Cu, Mn and O and the contrast of the O element is brighter than that in the corroded S phase, which indicates that the $Al_{20}Cu_2Mn_3$ nanoparticle is dissolved more severely than the S phase and an oxide is proposed to form. The enrichment of Cu in the corroded core is slight and much of the Al and Mn elements still exist in the corroded $Al_{20}Cu_2Mn_3$ nanoparticle, which means that $Al_{20}Cu_2Mn_3$ is only dissolved partially. Meanwhile, the S phase is already locally dissolved at the periphery. In the dissolved zone there is a lack of Al and Mg but it is enriched with Cu and O, which indicates that the S phase is decomposed by the selective dissolution of Al and Mg while Cu remains in the form of an oxide. From the images of Figs. 1, 2 and 6, it is seen that $Al_{20}Cu_2Mn_3$ is dissolved almost completely when the S phase is dissolved severely, from which we can deduce that the dissolution of $Al_{20}Cu_2Mn_3$ is continued parallel to the S phase dissolution.

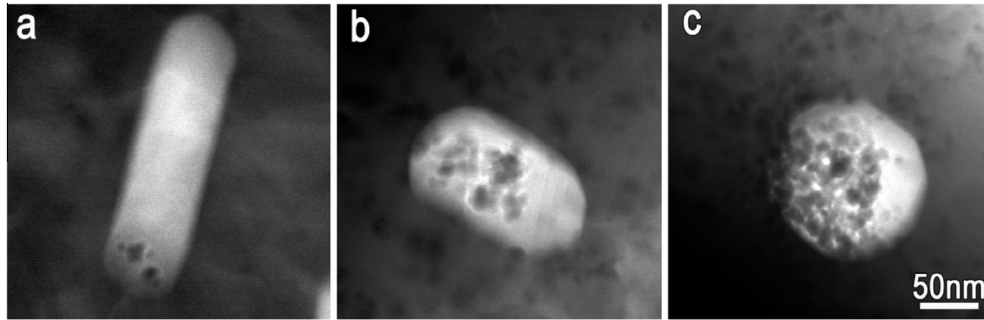**Fig. 7.** HAADF images showing three local-dissolved $Al_{20}Cu_2Mn_3$ particles distributed in Al matrix with varying degrees of corrosion.
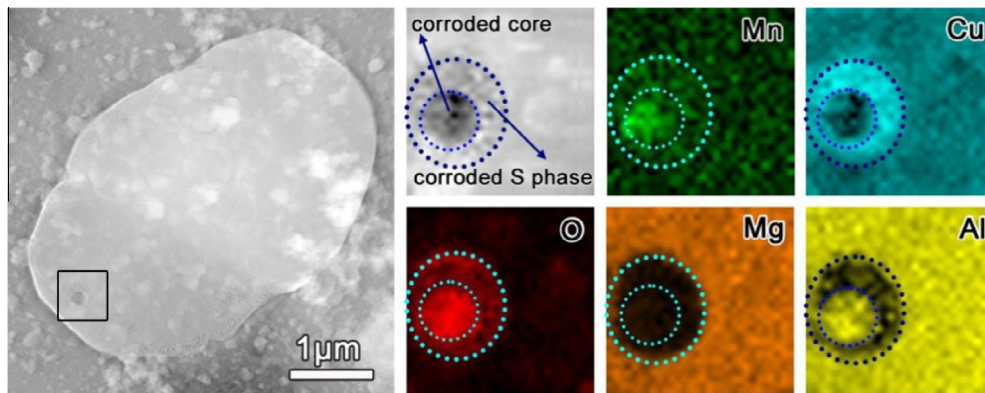


**Fig. 8.** HAADF image of a locally dissolved S phase and its EDS mapping on a pit.

Based on the discussion above, we hypothesize that local corrosion proceeds as follows: the S phase, $Al_{20}Cu_2Mn_3$ phase and Al matrix consist of a multi-galvanic couple. The S phase and $Al_{20}Cu_2Mn_3$ act as the anode and Al matrix cathode. The $Al_{20}Cu_2Mn_3$ phase is more active and dissolved initially. Although Cu enrichment occurs, the dissolution does not make $Al_{20}Cu_2Mn_3$ switch to cathodic, while it can create a local acid environment due to the hydrolysis of metal cations. The S phase anode, triggered by the local acid environment, becomes dissolved and enlarged. The local dissolved area in the S phase turns cathodic, which in turn accelerates the further dissolution of the adjacent $Al_{20}Cu_2Mn_3$. However, the $Al_{20}Cu_2Mn_3$ particles in the matrix have no chance to experience such a "self-catalyzing" like process and thus they are corroded slightly as an anode with respect to the Al matrix. When the local dissolution of the S phase extends to the boundary, the effect of the S phase (anodic)/Al matrix (cathodic) galvanic couple is prominent. Thus the dissolution develops along the boundary quickly and a Cu-rich remnant ring forms. When dealloying develops further, the Cu-rich ring changes from an anode to a cathode, which results in a local dissolution of the adjacent Al matrix and a parallel extending of S phase dissolution. Thus the prominent effect of the $Al_{20}Cu_2Mn_3$ phase is to indirectly influence the localized corrosion behavior of Al alloy through increasing the electrochemical activity of the S phase, other than directly impacting the Al matrix, which is one of the main reasons why the $Al_{20}Cu_2Mn_3$ phase has been neglected in electrochemistry in the past few decades.

### 3.3. Heterogeneous dissolution of $Al_{20}Cu_2Mn_3$

By observing numerous $Al_{20}Cu_2Mn_3$ particles, an inhomogeneous dissolution in the $Al_{20}Cu_2Mn_3$ particles is identified. In order to determine the detailed dissolution, we shorten the immersion duration to monitor the local dissolution at an initial stage. Fig. 9a is an HAADF image showing an S phase particle with some $Al_{20}Cu_2Mn_3$ embedding and Fig. 9b is the same particle which has been immersed in $0.5 \ mol \ l^{-1}$ NaCl for 8 min. By comparing these images, a darker contrast is seen at the inner part of an $Al_{20}Cu_2Mn_3$ nanoparticle (marked with arrow) after immersion, which indicates that the $Al_{20}Cu_2Mn_3$ particle is dissolved slightly while the S phase remains unchanged. Fig. 9c shows bright-field TEM images of the same $Al_{20}Cu_2Mn_3$ particle as in Fig. 9a. In contrast to the HAADF mode, which is more sensitive to chemical composition and/or thickness contribution, the bright-field mode shows more crystallographic details. It is seen that the $Al_{20}Cu_2Mn_3$ particle features multiple twins with a configuration of prism shaped plates and the initial site of preferential dissolution is in the vicinity of the intersected zone. Similarly, the dissolution activity of $Al_{20}Cu_2Mn_3$ particles is also found to be highly heterogeneous from one to another. As shown in Fig. 10a and b, in an S phase particle immersed in NaCl for 25 min, some $Al_{20}Cu_2Mn_3$ particles marked with black arrows are dissolved severely, around which the S phase is also decomposed. Moreover, the Al matrix at the S phase/Al interface is dissolved as well. Some other $Al_{20}Cu_2Mn_3$ particles labeled as I, II, III and IV, nevertheless, were not attacked, which indicates that $Al_{20}Cu_2Mn_3$ particles behave differently. Fig. 10c(I–IV) shows the zoom-in
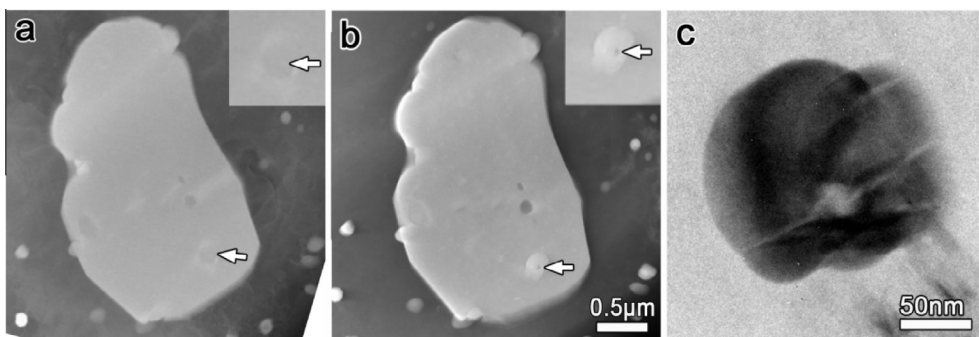
**Fig. 9.** Observation of the initial site where $Al_{20}Cu_2Mn_3$ begins to dissolve. (a) An HAADF image showing an S phase particle embedded with $Al_{20}Cu_2Mn_3$. (b) The same particle as that in (a) but suffering an immersion in 0.5 M NaCl solution for 8 min. One of the $Al_{20}Cu_2Mn_3$ is marked with an arrow and the zoom-in images are shown in the insert. (c) Bright-field TEM images of the $Al_{20}Cu_2Mn$ particles in (a).



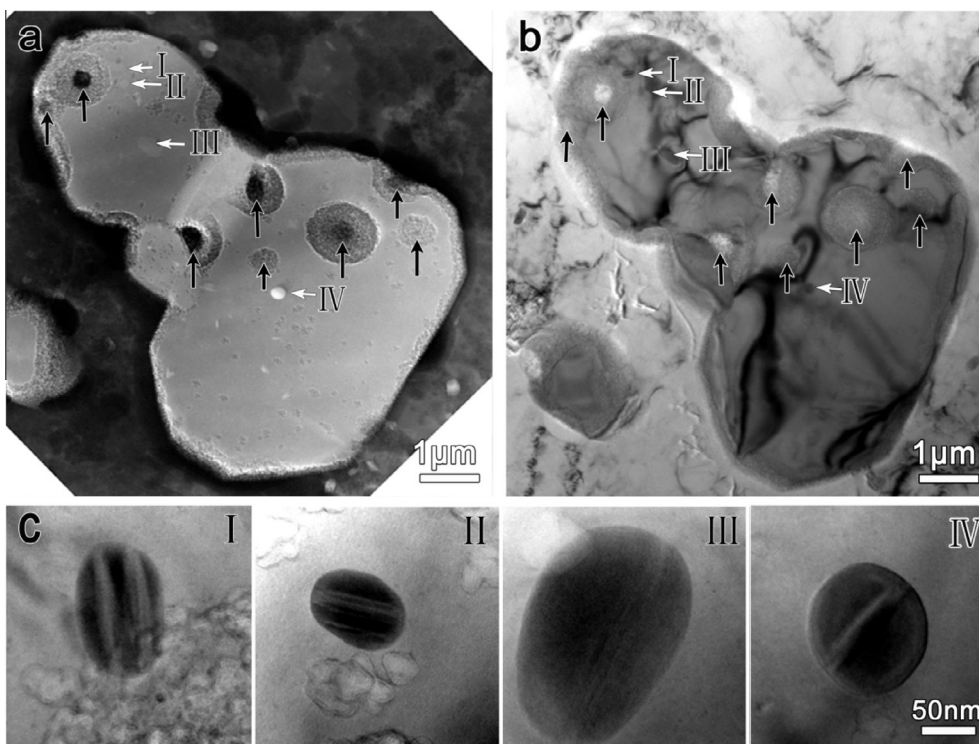**Fig. 10.** (a) HAADF image showing an S phase particle in which some $Al_{20}Cu_2Mn_3$ particles dissolve severely (marked with black arrows) and the S phase, even the Al matrix, also dissolves locally, while the other four particles labeled as I, II, III and IV have no change. The specimen was immersed in 0.5 mol $l^{-1}$ NaCl for 25 min. (b) Bright-field TEM image corresponding to (a). (c) Zoom-in TEM images of the particles I, II, III and IV.

images of the four undissolved $Al_{20}Cu_2Mn_3$ particles in Fig. 10b. It can be seen that these particles feature only simple parallel twins. By observation of numerous $Al_{20}Cu_2Mn_3$ particles in the S phase, some other undissolved $Al_{20}Cu_2Mn_3$ particles free of twinning were also observed (not shown here). Meanwhile, we find a large number of $Al_{20}Cu_2Mn_3$ particles in the Al matrix which are slightly dissolved, typically shown in Fig. 11. All these particles feature multiple twins and are preferentially dissolved in the vicinity of the intersected zone of the prism twin plates or at the center of multi-parallel shaped twin plates. The difference in the configuration of twins existing in the $Al_{20}Cu_2Mn_3$ phase is responsible for the heterogeneous activity. In other words, those with multiple twins behave active and are dissolved preferentially in the vicinity of the intersected zone, while those free of twins or with simple

parallel twins are inactive and undissolved even though dissolution occurs in some S phase particles.

Efforts were made to synthesize the bulk intermetallic second phases and the electrochemical behaviors were measured by Leard and Buchheit [34]. The electrochemical activities of these intermetallics were labeled in the following order: $Al_2CuMg$ (S phase) > $Al_2Cu$ (θ phase) > $Al_7Cu_2$ Fe > $Al_{20}Cu_2Mn_3$, which indicates that $Al_{20}Cu_2Mn_3$ is the most stable phase while the S phase is the most active one. Birbilis et al. [35] and Ilevbare and Scully [36] also noted the $Al_{20}Cu_2Mn_3$ as functioning as potent local cathodes. Furthermore, evident attack is always found to begin at the S phase at the macro-scale. Thus in the past a few decades, much attention was paid to the S phase in the study of pitting in 2024Al alloy, while little attention was paid to the $Al_{20}Cu_2Mn_3$ phase. The present study updates

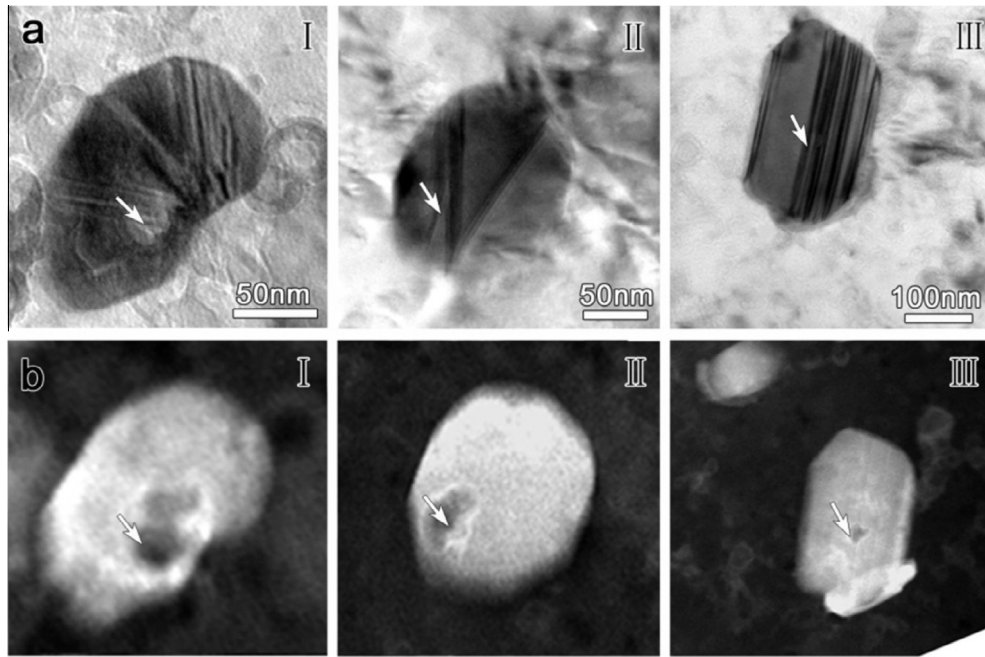**Fig. 11.** Twins in $Al_{20}Cu_2Mn_3$ provide the initial dissolution sites. (a) Bright-field TEM images of $Al_{20}Cu_2Mn_3$ particles showing the feature of twins in $Al_{20}Cu_2Mn_3$. (b) HAADF images of the same particles showing the initial site of dissolution in $Al_{20}Cu_2Mn_3$. The specimen was immersed in $0.5$ mol $l^{-1}$ NaCl for 25 min.

the activity order of the main second phase as: $Al_{20}Cu_2Mn_3$ (with multiple twins) > S phase > $Al_{20}Cu_2Mn_3$ (without twins or with simple parallel twins), which is remarkably different from the previous viewpoint. However, the $Al_{20}Cu_2Mn_3$ which was used for investigation in the above research was synthesized artificially, rather than using a dispersoid precipitated in alloys. As a result, the composition and microstructural configuration in the as-synthesized $Al_{20}Cu_2Mn_3$ are proposed to be different from the dispersoid precipitations in the present 2024Al alloy, which may significantly influence the electrochemical properties. Thus, the cathodic property of as-synthesized $Al_{20}Cu_2Mn_3$ cannot be representative of that precipitated in industrial Al alloys.

The phenomenon that $Al_{20}Cu_2Mn_3$ with multiple twins is more active than those free of twins implies that a special structure or chemical composition may exist at the intersected zone of twins, which changes the electrochemical activity. The microstructure of $Al_{20}Cu_2Mn_3$ is similar with the T–Al–Pd–Mn and Al–Pd–Fe phases in which the metadislocations were observed in previous studies [37,38]. Metadislocations are known to be very complex defects in crystals as they usually involve several hundreds of atoms in their core. The metadislocations are proposed to exist in the present $Al_{20}Cu_2Mn_3$ approximant and probably they prefer to form at the intersected zone of twin plates. The heterogeneous dissolution activity of $Al_{20}Cu_2Mn_3$ particles in the present study might be more or less associated with the metadislocations to be confirmed further.

## 4. Conclusions

With the application of in situ ex-environmental TEM, we have identified the initial site, at an atomic scale, of pitting corrosion in an Al–Cu–Mg alloy. The S-$Al_2CuMg$ phase is compositionally and structurally inhomogeneous.

A large number of nanosized approximants of the DQC, which is determined to be $Al_{20}Cu_2Mn_3$, are embedded in most S particles. TEM studies indicate that the embedded $Al_{20}Cu_2Mn_3$ approximants are responsible for the activity of the S phase, which clarifies the well-known phenomenon that the activities of the S phase particles are electrochemically different from one to another. In addition, we have directly observed that the dissolution of $Al_{20}Cu_2Mn_3$ approximant is the initial stage prior to the S phase dissolution. Moreover, we also find the initial site of the $Al_{20}Cu_2Mn_3$ dissolution and the electrochemical activity of different $Al_{20}Cu_2Mn_3$ particles is varied. The $Al_{20}Cu_2Mn_3$ approximants with multiple twins are more active than those with few planar defects.

## References

[1] S.C. Wang, M.J. Starink, Int. Mater. Rev. 50 (2005) 193.
[2] S. Cheng, Y.H. Zhao, Y.T. Zhu, E. Ma, Acta Mater. 55 (2007) 5822.
[3] A. Hughes, T.H. Muster, A. Boag, A.M. Glenn, C. Luo, X. Zhou, et al., Corros. Sci. 52 (2010) 665.
[4] R. Wei, C.-M. Liao, M. Gao, Metall. Mater. Trans. A 29 (1998) 1153.
[5] W. Zhang, G.S. Frankel, Electrochim. Acta 48 (2003) 1193.
[6] C. Blanc, A. Freulon, M.-C. Lafont, Y. Kihn, G. Mankowski, Corros. Sci. 48 (2006) 3838.
[7] L. Lacroix, L. Ressier, C. Blanc, G. Mankowski, J. Electrochem. Soc. 155 (2008) C131.

[8] C. Augustin, E. Andrieu, C. Blanc, G. Mankowski, J. Delfosse, J. Electrochem. Soc. 154 (2007) C637.

[9] A. Boag, A.E. Hughes, A.M. Glenn, T.H. Muster, D. McCulloch, Corros. Sci. 53 (2011) 17.

[10] R.G. Buchheit, R.P. Grant, P.F. Hlava, B. McKenzie, G.L. Zender, J. Electrochem. Soc. 144 (1997) 2621.

[11] V. Guillaumin, G. Mankowski, Corros. Sci. 41 (1998) 421.

[12] D. Zhu, W.J. van Ooij, Corros. Sci. 45 (2003) 2177.

[13] N. Birbilis, R.G. Buchheit, D.L. Ho, M. Forsyth, Electrochem. Solid State Lett. 8 (2005) C180.

[14] M. Bethencourt, F.J. Botana, M.J. Cano, M. Marcos, J.M. Sanchez-Amaya, L. Gonzalez-Rovira, Corros. Sci. 51 (2009) 518.

[15] A. Boag, R.J. Taylor, T.H. Muster, N. Goodman, D. McCulloch, C. Ryan, et al., Corros. Sci. 52 (2010) 90.

[16] V. Radmilovic, R. Kilaas, U. Dahmen, G.J. Shiflet, Acta Mater. 47 (1999) 3987.

[17] J. Majimel, G. Molenat, F. Danoix, O. Thuillier, D. Blavette, G. Lapasset, et al., Philos. Mag. 84 (2004) 3263.

[18] S.C. Wang, M.J. Starink, Acta Mater. 55 (2007) 933.

[19] Z.R. Liu, J.H. Chen, S.B. Wang, D.W. Yuan, M.J. Yin, C.L. Wu, Acta Mater. 59 (2011) 7396.

[20] H. Perlitz, A. Westgten, Arkiv. Kemi. Mineral. Geol. 16B (1943) 13.

[21] R. Kilaas, V. Radmilovic, Ultramicroscopy 88 (2001) 63.

[22] H.M. Obispo, L.E. Murr, R.M. Arrowood, E.A. Trillo, J. Mater. Sci. 35 (2000) 3479.

[23] L. Lacroix, L. Ressier, C. Blanc, G. Mankowski, J. Electrochem. Soc. 155 (2008) C8.

[24] S.J. Zheng, Y.J. Wang, B. Zhang, Y.L. Zhu, C. Liu, P. Hu, et al., Acta Mater. 58 (2010) 5070.

[25] S.J. Pennycook, Structure determination through Z-contrast microscopy, in: P.W. Hawkes, V.-A. Marco (Eds.), Advances in Imaging and Electron Physics, vol. 123, Elsevier, Amsterdam, 2002, p. 173.

[26] J.D. FitzGerald, R.L. Withers, A.M. Stewart, A. Calka, Philos. Mag. B58 (1988) 15.

[27] R.C. Hudd, W.H. Taaylor, Acta Crystallogr. 15 (1962) 271.

[28] K. Robinson, Philos. Mag. 43 (1952) 775.

[29] K. Robinson, Acta Crystallogr. 7 (1954) 494.

[30] S.C. Wang, C.Z. Li, M.G. Yan, Mater. Res. Bull. 24 (1989) 1267.

[31] X.Z. Li, K.H. Kuo, Philos. Mag. B 66 (1992) 117.

[32] Y. Li, Z. Liu, L. Lin, J. Peng, A. Ning, J. Mater. Sci. 46 (2011) 3708.

[33] A.R. Toleuova, N.A. Belov, D.U. Smagulov, A.N. Alabin, Met. Sci. Heat Treat. 54 (2012) 402.

[34] R.R. Leard, R.G. Buchheit, Electrochemical characterization of copper-bearing intermetallic compounds and localized corrosion of Al–Cu–Mg–Mn alloy 2024, in: P.J.H.S.J. Gregson (Ed.), Aluminum Alloys 2002: Their Physical and Mechanical Properties, Pts. 1–3, vol. 396–4, Trans Tech Publications Ltd, Switzerland, 2002, p. 1491.

[35] N. Birbilis, M.K. Cavanaugh, R.G. Buchheit, Corros. Sci. 48 (2006) 4202.

[36] G.O. Ilevbare, J.R. Scully, Corrosion 57 (2001) 134.

[37] M. Heggen, L. Houben, M. Feuerbacher, Nat. Mater. 9 (2010) 332.

[38] M. Heggen, L. Houben, M. Feuerbacher, Philos. Mag. 88 (2008) 2333.